Nanoscale

PAPER

View Article Online
View Journal

Cite this: DOI: 10.1039/d6nr00201c

Atomically thin CVD graphene-integrated proton exchange membrane electrode assemblies: fabrication parameter space and hydrogen crossover mitigation

Xiaozong Fan,[a] Aman Tamboli,[a] Pavan Chaturvedi,[a] Rafiq Ahmed,[a] Anusorn Kongkanand[b] and Piran R. Kidambi *[c,d,e]

Proton selective, atomically thin two-dimensional (2D) materials interfaced with state-of-the-art proton exchange membranes (PEMs) enable overcoming the inherent trade-off between proton conductance and gas crossover. Monolayer graphene-integrated PEMs show significantly reduced gas crossover with negligible impact on proton conductance. However, the influence of fabrication methods on membrane–electrode assemblies (MEAs) using PEMs interfaced with monolayer graphene (synthesized *via* chemical vapor deposition (CVD)) *via* an ultra-thin (~700 nm) ionomer carrier layer remains elusive. Here, we systematically investigate three MEA fabrication processes: gas diffusion electrode (GDE), directly sprayed catalyst-coated membrane (DS-CCM), and decal transfer catalyst-coated membrane (DT-CCM) using monolayer CVD graphene-integrated with perfluorosulfonic acid (PFSA) PEMs (~12–25 μm thick). Although the GDE process minimizes processing or impact on PEM properties, the rough surface of the GDE could damage CVD graphene coated with the ~700 nm ionomer carrier layer, limiting the suppression of H_2 crossover. The DS-CCM approach exposes the PEM to solvents, resulting in degradation and diminished performance. DT-CCM emerges as the most effective route, with minimal graphene damage, yielding a pronounced reduction (~25–44%) in H_2 crossover without impacting proton conductance. Notably, the decal approach remains effective even for thinner (~12 μm thick) PEMs with inherently higher proton conductance, where reduced crossover can enable enhanced membrane durability and fuel cell efficiency. These findings establish fabrication-sensitive design rules for integrating 2D materials into MEAs and highlight the advantages of the decal-transfer approach for next-generation PEMs.

Received 15th January 2026,
Accepted 9th April 2026

DOI: 10.1039/d6nr00201c

rsc.li/nanoscale

Introduction

Proton exchange membranes (PEMs)[1–4] govern the efficiency, durability, and operating envelope of electrochemical energy-conversion devices, including proton exchange membrane fuel cells and electrolyzers.[2,5–14] State-of-the-art perfluorosulfonic acid membranes such as Nafion achieve high proton conductivity through hydrated ionic domains; however, their gas barrier properties scale inversely with thickness.[15] As a result, membrane thinning—an established strategy for reducing ohmic losses and enhancing power density—inevitably leads to increased hydrogen and oxygen crossover, which accelerates chemical degradation, induces parasitic reactions, and limits device lifetime.[15] Overcoming this intrinsic conductivity–permeability trade-off remains a central challenge in PEM design.[1,3,4,15–20]

Atomically thin two-dimensional (2D) materials have recently emerged as interfacial layers capable of decoupling proton transport from molecular gas permeation.[1,3,4,16–19,21–23] In particular, monolayer graphene synthesized *via* scalable chemical vapor deposition (CVD) enables selective proton permeation *via* angstrom-scale intrinsic lattice defects while simultaneously hindering H_2 crossover.[1,3,4,17,18] CVD graphene-integrated with a PFSA membrane offers the opportunity to introduce an ultrathin, proton-selective gas crossover suppression layer without adding measurable ionic resistance.[1,3,4,17,18,24] While these properties have been demonstrated at the material and membrane levels, translation to functional devices requires fabrication of membrane–electrode

[a]Department of Chemical and Biomolecular Engineering, Vanderbilt University, Nashville, TN, USA
[b]Fuel Cell Business, General Motors, Pontiac, Michigan 48340, USA
[c]Department of Mechanical and Aerospace Engineering, University of Florida, FL 32611, USA. E-mail: p.kidambi@ufl.edu
[d]Department of Chemical Engineering, University of Florida, FL 32611, USA
[e]Department of Materials Science and Engineering, University of Florida, FL 32611, USA

assemblies (MEAs) while preserving both graphene structural integrity and PFSA membrane properties.[1,5,6,8–15,19,21,25–36]

However, the influence of MEA fabrication methods on monolayer CVD graphene interfaced with a PFSA membrane *via* an ultra-thin (~700 nm) carrier layer remains to be understood.[1–4,17,18,37,38] Although, the ultra-thin carrier layer approach alleviates increased thickness from sandwiching CVD graphene between two idividual PFSA membranes, the membrane electrode assembly (MEA) fabrication involves a complex interplay of mechanical compression, surface roughness (1–10 μm), solvent exposure, and interfacial adhesion—all of which can introduce defects in CVD graphene[1,3,6,18,26,30,32,33,36–74] or alter membrane structure/properties.[15] Given that gas permeation through graphene is extremely sensitive to nanoscale defects, even minor mechanical or chemical damage during MEA fabrication can negate its barrier functionality, underscoring the need for fabrication-sensitive integration strategies.[2,3,18,38,45,56,75]

Here, we systematically evaluate three technologically relevant MEA fabrication approaches—the use of a gas diffusion electrode (GDE), a directly sprayed catalyst-coated membrane (DS-CCM), and a decal transfer catalyst-coated membrane (DT-CCM)—for incorporating CVD-grown monolayer graphene into MEAs with membrane thicknesses ranging from ~12 to 25 μm. The GDE approach largely preserves membrane properties; however, the intrinsic surface roughness of GDEs and the resulting mechanical stresses from hot pressing can induce tearing or cracking of the ~700 nm thin PFSA ionomer coated CVD graphene layer, thereby limiting the suppression of hydrogen crossover. Conversely, DS-CCM fabrication involves solvent-based catalyst deposition directly onto the membrane, which can degrade PEM properties.

We identify decal transfer (DT-CCM) as the most effective approach that minimizes both mechanical damage to ~700 nm thin ionomer coated CVD graphene and solvent exposure of the membrane. The decal transfer process enables a significant reduction (~25–44%) in H_2 crossover without compromising proton conductance. Importantly, the benefits of DT-CCM graphene persist for thinner (~12 μm) membranes with inherently higher proton conductivity, where suppressed gas crossover directly mitigates chemical degradation pathways and enhances membrane durability.

Results and discussion

Centimeter-scale CVD graphene was grown on Cu foil and integrated with PEMs (12–25 μm) using an ~700 nm thin spin-coated Nafion carrier layer (Fig. 1A), followed by the removal of the Cu foil using ammonium persulfate solution (see the Methods section). The Raman spectrum with a characteristic 2D peak at ~2700 cm^{-1} and a G peak ~1600 cm^{-1}, and the absence of a D peak indicates high-quality graphene while $I_{2D}/I_G > 1$ confirms the monolayer film (see Fig. 1A).[17,62,69] CVD graphene-integrated PEMs were used to fabricate MEAs using three different approaches: 1) the use of a gas diffusion electrode (GDE), 2) a directly sprayed catalyst-coated membrane (DS-CCM), and 3) a decal transfer catalyst-coated membrane (DT-CCM) (Fig. 1B; see the Methods section for details).

To investigate the impact of fabrication methods on the MEAs, we tested them using standard fuel cell tests using a single-cell test station (see the Methods section). First, we evaluate the fuel cell performance of MEAs with bare N211 membranes (~25 μm-thick Nafion® membrane) prepared using the GDE, DS-CCM, and DT-CCM approaches (Fig. 2, Table 1).

Interestingly, all three MEA fabrication approaches show similar polarization curves with minor differences of ~10% (Fig. 2A) *i.e.,* the MEA with the GDE had a power density of ~852 mW cm^{-2} (at 0.6 V), while the DS-CCM showed ~769 mW cm^{-2} (at 0.6 V) and the DT-CCM was in between at ~784 mW cm^{-2} (at 0.6 V). The observed similarity in the cell power densities is also reflected in similar high-frequency resistance (HFR) values in the ~61–65 mΩ cm^2 range (Fig. 2F). Parameters such as electrochemically active surface area (ECSA) also affect the cell power density. The GDE and DT-CCM samples exhibited comparable (35 *vs.* 37 m^2 g^{-1}) ECSAs (Fig. 2E) whereas DS-CCM exhibited a lower value (23 m^2 g^{-1}). We attribute the estimated lower ECSA value of DS-CCM to challenges in accurate determination of Pt loading (~0.2 mg) using the difference in weight for a small active area of 1 cm^2, especially when the catalyst ink is sprayed manually onto moisture-sensitive PEMs.

The cell open-circuit voltages (OCVs, Fig. 2D) also show similar values with that for the GDE being marginally higher,

Piran R. Kidambi

Piran R. Kidambi is an associate professor in Mechanical and Aerospace Engineering with affiliate appointments in Chemical Enigneering and Material Science at the University of Florida. After receiving his PhD from the University of Cambridge, he pursued postdoctoral research at MIT through a Lindemann Trust fellowship. Kidambi's research leverages the intersection between (i) nanomaterial synthesis, (ii) process engineering, and (iii) in situ metrology, to enable bottom-up materials design and synthesis for energy, separations, and healthcare applications. His research has been recognized via several awards and honors including ASME Rising Star (2024), 2024 Donald D. Harrington Faculty Fellowship at the University of Texas at Austin, AIChE NSEF Young Investigator (2023), DOE Early Career Award (2022), ACS PMSE Young Investigator (2022), NSF CAREER (2020), ECS Toyota Young Investigator (2020), and Ralph E. Powe Junior Faculty Award (2018), among others.

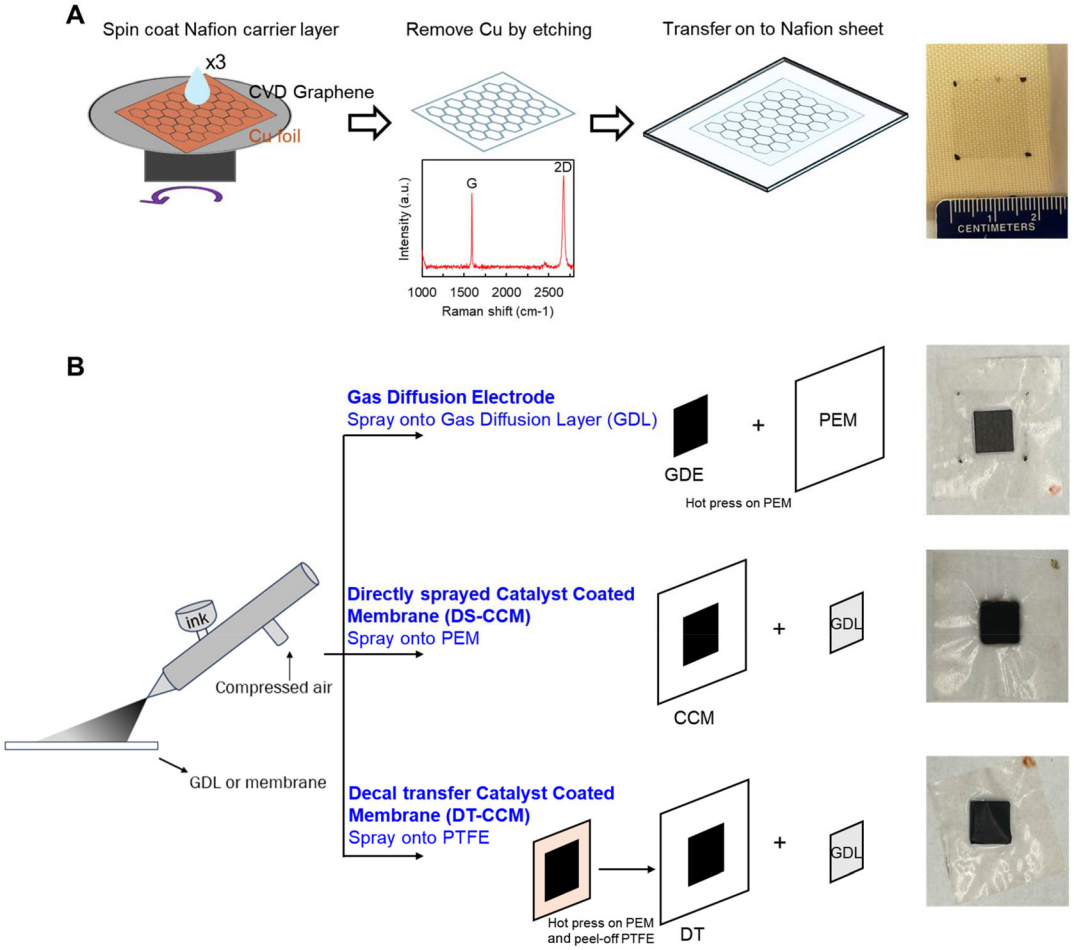

Fig. 1 (A) Schematic of the spin-scoop method to integrate CVD graphene with Nafion using a ~700 nm thin ionomer carrier layer. Inset shows the Raman spectrum for CVD graphene consistent with that of a high-quality monolayer. (B) Schematic of the approaches used to prepare the membrane-electrode assemblies (MEAs): 1) the use of gas diffusion electrode (GDE), 2) directly sprayed catalyst-coated membrane (DS-CCM), and 3) decal transfer catalyst-coated membrane (DT-CCM).

while those of DT-CCM and DS-CCM were essentially identical. Notably, all the cell OCVs were >950 mV, suggesting good integrity of the fabricated MEAs. However, significant differences were observed in the crossover current density (Fig. 2B and C): the GDE exhibited the lowest value (~2.56 mA cm^{-2}), followed by DT-CCM (~3.46 mA cm^{-2}), and DS-CCM showed the highest (~4.01 mA cm^{-2}).

This trend can be attributed to the fabrication-dependent effects on the membrane. Specifically, in the case of DS-CCM, direct spraying of the catalyst ink onto the membrane could have resulted in mechanical stress (from swelling and drying) from residual solvent (water–alcohol mixtures) as well as process-dependent drying characteristics (compared to DT-CCM sprayed with PTFE while keeping holder temperature the same). Such differences could have potentially led to structural defects and thereby causing high H_2 crossover. However, these issues are largely absent in the DT-CCM and GDE samples, which avoid direct solvent–membrane interaction, albeit the DT-CCM approach involves more hot-pressing steps in MEA fabrication compared to the GDE. We note the small active area (1 cm^2) cell used in this study has a relatively high edge-to-active-area ratio and can potentially lead to higher H_2 crossover when the membrane edge integrity is compromised mechanically (hot press) or from solvent interaction. The above analysis suggests that MEA fabrication with a bare membrane *via* the GDE emerges as the most effective method, followed by DT-CCM.

Since the GDE exhibited the highest cell power density (Fig. 2A) with the least hydrogen crossover (Fig. 2B and C), we proceeded to fabricate MEAs with the GDE using slow-growth CVD graphene (SG; see the Methods section) integrated PEMs (N211 + SG or N12 + SG shown in Fig. 3). Standard fuel cell tests suggest similar polarization curves for membranes with and without graphene (Fig. 3A) in the high- and mid-potential regions but differed at low potentials. The slightly lower performance of the N211 + SG sample at low potentials is within test variation due to gas bypass in our oversized flow fields. A minimal increase in membrane resistance is observed from HFR, which appears promising at first (Fig. 3F). The bare N211 GDE exhibits an ECSA of ~35 m^2 g^{-1}, which is a slightly lower

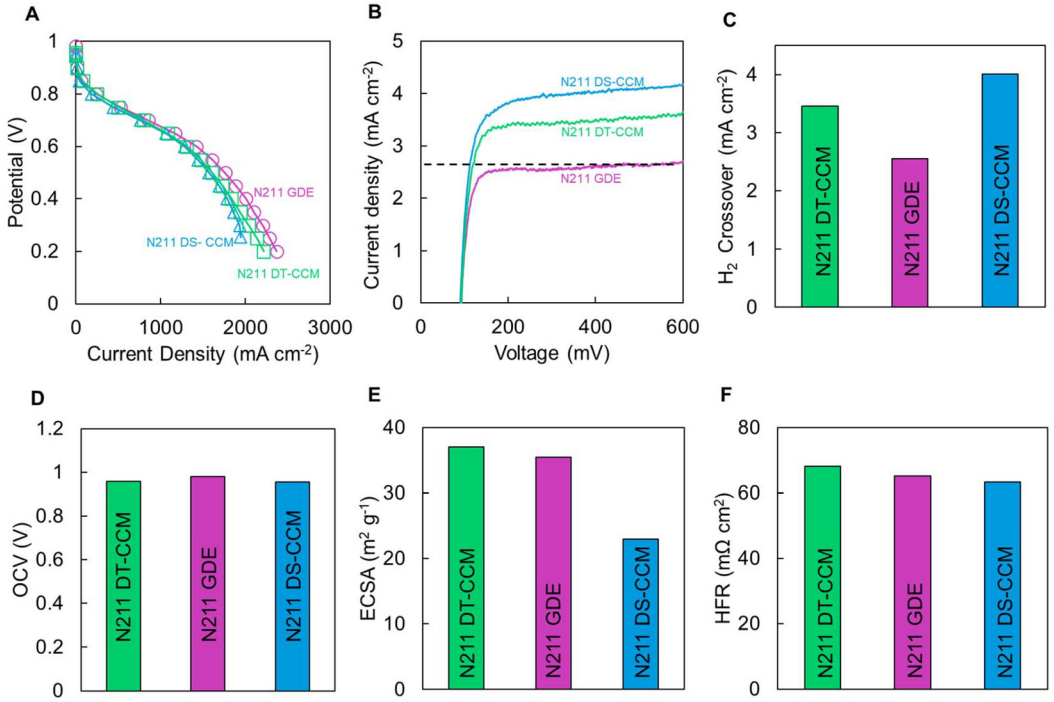

Fig. 2 Fuel-cell performance of MEAs comprising N211 control membranes (without a spin-scoop layer) fabricated using a gas diffusion electrode (GDE), directly sprayed catalyst-coated membrane (DS-CCM), and decal transfer catalyst-coated membrane (DT-CCM) using 80 °C, 100% RH and 150 kPa_{abs}. (A) Polarization curves, (B) crossover current density as a function of voltage, and (C) H_2 crossover extracted from (B) at 0.4 V. (D) Open-circuit voltage (OCV), (E) electrochemically active surface area (ECSA), and (F) high-frequency resistance (HFR) obtained at 1000 mA cm^{-2}. The dotted line in (B) shows the theoretical value for H_2 crossover for N211 PEMs, which agrees well with that of N211 MEA fabricated using the GDE approach. Also see Table 1.

Table 1 Summary of data from Fig. 1 for MEAs comprising N211 control membranes

	OCV (V)	ECSA (m^2 g^{-1})	HFR at 1000 mA cm^{-2} (mΩ cm^2)	H_2 crossover (mA cm^{-2})
N211 GDE	0.981	35	65	2.56
N211 DS-CCM	0.956	23	63	4.01
N211 DT-CCM	0.957	37	68	3.46

value compared to that of N211 + SG of ~41 m^2 g^{-1}, although the difference remains within a reasonable range for ECSA measurements. However, we did not observe any reduction in hydrogen crossover with the incorporation of graphene (N211 GDE + SG, Fig. 3B and C, Table 2) compared to the bare PEM (N211 GDE, Fig 3B and C, Table 2).

Specifically, the H_2 crossover current density of the N211 GDE +SG sample of ~2.44 mA cm^{-2} was < 5%, as that of the bare N211 GDE ~2.56 mA cm^{-2}, indicating that the CVD graphene layer did not significantly affect H_2 crossover. We hypothesize that this lack of crossover reduction arises from the penetration of the rough GDE surface through the ~700 nm-thin layer of spin-coated Nafion carrier layer, damaging the CVD graphene and diminishing its barrier properties. Similarly, the MEAs prepared with the N12 membrane (12 μm thick PFSA membrane with an internal reinforcement layer, see methods section) and GDEs showed no noticeable change in polarization performance (Fig. 3A) or crossover reduction (Fig. 3B and C, and Table 2). These consistent results for both N211 and N12 membranes suggest that the absence of improvement is primarily due to the GDE fabrication process compromising the integrity of the CVD graphene layer, rather than differences in the intrinsic properties of the Nafion membranes.

We note that even state-of-the-art GDEs have relatively high surface roughness with a mean surface roughness (R_a) of ~ 2 μm. Hence, it is reasonable that the high surface roughness of the GDE can damage the graphene layer through the 700 nm ionomer carrier film depending on the fabrication parameters.

Furthermore, during hot-pressing, the stack of MEA sub-components are heated to around the glass transition temperature of the Nafion in order to soften it. As shown in Fig. 4C, we investigated this issue by systematically varying the temperature and pressure of the GDE process for MEAs using PEMs with and without CVD graphene. When the GDEs were hot-pressed at lower temperatures and pressures (120 °C and 125 psi), the effect of the CVD graphene becomes more evident, yielding approximately a 19% reduction in crossover. In contrast, at higher temperatures and pressures (*e.g.* 150 °C and 250 psi or 140 °C and 1000 psi), the CVD graphene layer provided no reduction in H_2 crossover in comparison with the

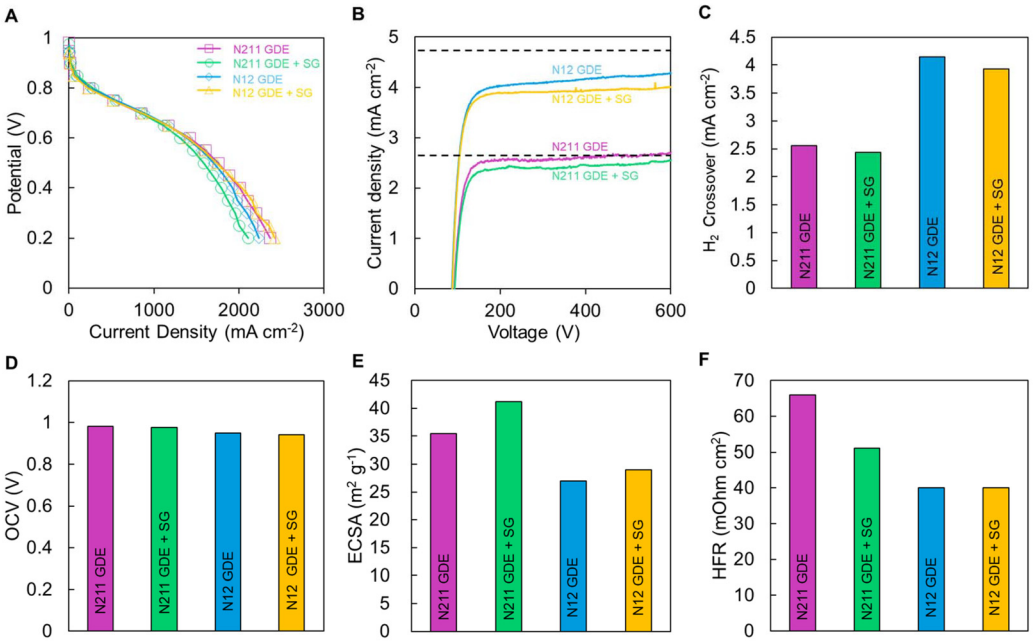

Fig. 3 Fuel cell performance of MEAs fabricated with GDEs using Nafion N211 (~25 μm thick) or N12 (~12 μm thick) bare membranes as well as with CVD graphene-integrated PEMs (N211 + SG or N12 + SG) using 80 °C, 100% RH and 150 kPa_{abs}. (A) Polarization curves, (B) crossover current density as a function of voltage, and (C) H_2 crossover extracted from (B) at 0.4 V. (D) Open-circuit voltage (OCV), (E) electrochemically active surface area (ECSA), and (F) high-frequency resistance (HFR) at 1000 mA cm^{-2}. The dotted line in (B) shows the theoretical value for H_2 crossover for N211 and N12 PEMs. Also see Table 2.

Table 2 Summary of data from Fig. 3 for MEAs fabricated using the GDE method

	OCV (V)	ECSA (m^2 g^{-1})	HFR at 1000 mA cm^{-2} (mΩ cm^2)	H_2 crossover (mA cm^{-2})
N211 GDE	0.981	35	65	2.56
N211 + SG GDE	0.975	41	51	2.44
N12 GDE	0.947	27	40	4.14
N12 + SG GDE	0.941	29	40	3.93

control membranes. The reduction in crossover observed for the GDE samples under lower temperature and pressure hot-pressing conditions is consistent with the hypothesis that GDE-based MEAs benefit from the intimate contact formed among the PEM, catalyst layer, and GDL during hot pressing. Because the catalyst layers with rougher surfaces in the GDE samples were supported on a relatively stiff carbon fiber GDL, the applied pressure was efficiently transmitted to the membrane. In contrast, the decal electrodes in the DT-CCM samples were supported by a much smoother PTFE sheet. PTFE also softens at similar temperatures during hot-pressing, which allows it to alleviate the electrode roughness. Consequently, under identical hot-pressing conditions, the GDE MEAs were more likely to experience damage to CVD graphene compared to DT-CCM (Fig. 4C).

Cross-section SEM images (Fig. 4A) indeed confirm the rough GDE surface intruding into the PEM up to several microns. Furthermore, the GDE samples (Fig. 4A) exhibited a compacted, well-adhered catalyst–membrane interface, while the DT-CCM samples (Fig. 4B) show some voids, cracks, and local delamination. Such interfacial and structural defects provide additional pathways for gas transport, allowing hydrogen to bypass the catalyst layer and reach the membrane more easily. This explains why the GDE samples show lower crossover than the DT-CCM samples but exhibit only negligible additional suppression of crossover when incorporating CVD graphene under the same hot-pressing conditions.

Next, we examined DT-CCM-based MEAs with and without CVD graphene in single cell fuel cell tests under standard conditions (80 °C, 100% RH under a backpressure of 150 kPa_{abs}) (Fig. 5). We emphasize that the DT-CCM process required specific temperature, pressure, and time (250 psi, 150 °C, and 3 min, respectively) for optimal transfer of the catalyst ink sprayed on a PTFE sheet onto the PEM. Hence, we used identical parameters for the GDE-based MEA in Fig. 3 to facilitate a direct comparison and note that optimizing the GDE process parameters enables some improvements as shown in Fig. 4C. Furthermore, we also used commercially available CVD graphene (GG) in the DT-CCM approach to benchmark performance and to alleviate concerns regarding scalability as well as test the translatability of our processes (Fig. 5).

MEAs prepared using DT-CCM with and without CVD graphene showed similar polarization curves (Fig. 5A) with cell power density (~10% variation) for all the membranes *i.e.* bare N211 ~784 mW cm^{-2}, N211 with a spin-scoop Nafion carrier layer ~872 mW cm^{-2}, N211 + GG ~834 mW cm^{-2}, and N211 + SG ~831 mW cm^{-2}. The HFRs (Fig. 5F) of the MEAs were in

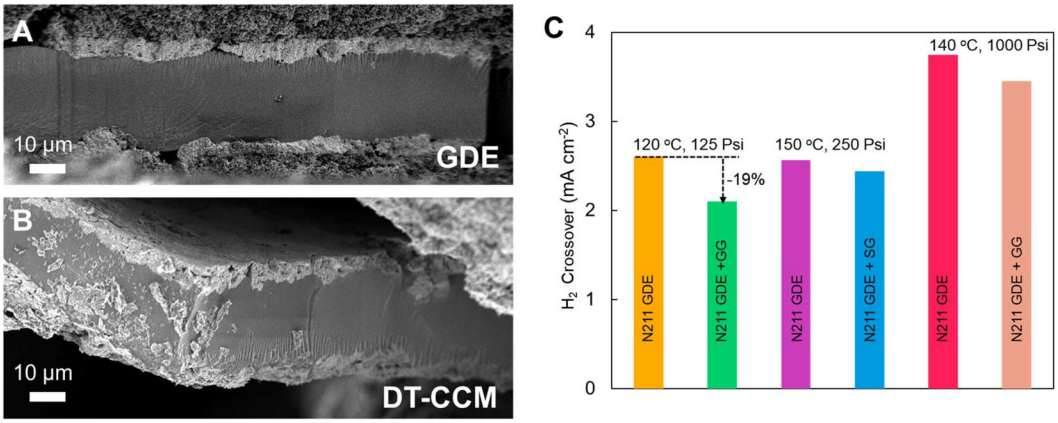

Fig. 4 Cross-sectional SEM images of (A) the GDE and (B) DT-CCM on N211 membrane. (C) H_2 crossover values for N211 spin-scoop (control) membranes and N211 spin-scoop with graphene (SG as well as GG - see methods section) using the GDE method of fabrication prepared under different hot-pressing conditions under 80° C, 100% RH and 150 kPa_{abs} conditions.

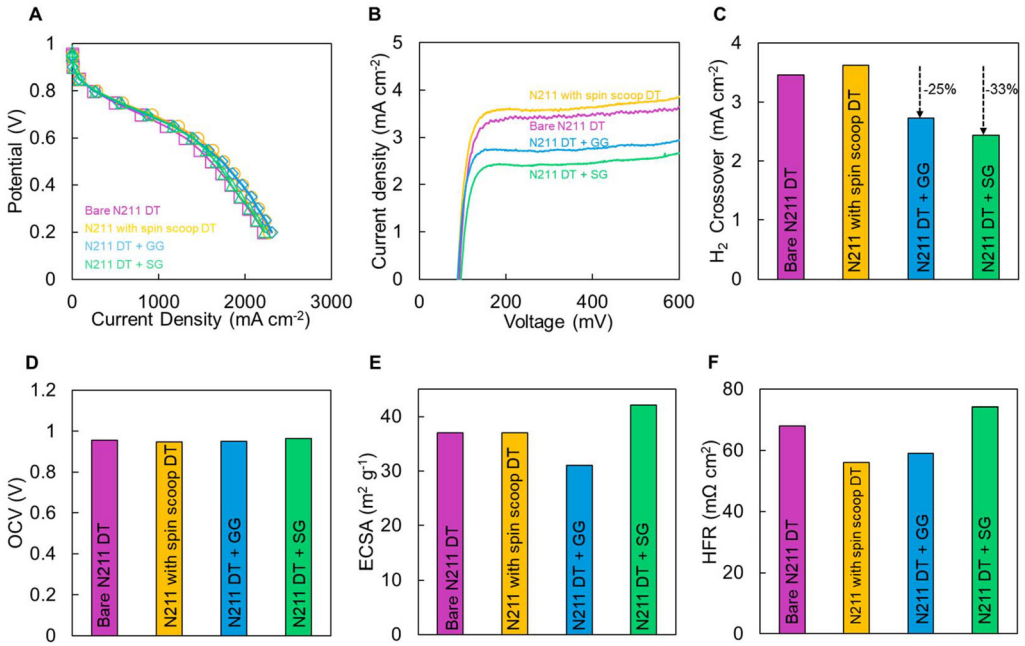

Fig. 5 Comparison of fuel cell performance under 80 °C, 100% RH and 150 kPa_{abs} conditions among MEAs with bare N211 membranes, N211 with spin-scoop carrier layer, N211 + GG (commercial CVD graphene), and N211 + SG (lab-grown CVD graphene) prepared using decal transfer (DT-CCM): (A) polarization curves, (B) current density as a function of voltage, and (C) H_2 crossover extracted from (B) at 0.4 V. (D) Open-circuit voltage (OCV), (E) electrochemically active surface area (ECSA), and (F) high-frequency resistance (HFR) at 1000 mA cm^{-2}. Note that DT-CCM is abbreviated as DT in this figure. Also see Table 3.

the range of ~58 to 74 mΩ cm^2 and the estimated ECSA (Fig. 5E) for N211 and N211 with the spin-scoop showing similar values (~37 m^2 g^{-1}), while N211 + SG exhibited a slightly higher ECSA (~42 m^2 g^{-1}) and N211 + GG showed a somewhat lower value (~31 m^2 g^{-1}). To understand the cell integrity, we tested the cell OCV and found all DT-CC based MEAs exhibited good cell integrity with the bare N211 showing an OCV value of ~0.957 V, N211 with the spin-scoop Nafion carrier layer of ~0.948 V, and N211 + SG showing a slightly higher value of ~0.966 V (Fig. 5D and Table 3). Notably, the H_2 crossover values (Fig. 5B and C) of ~2.73 for DT-CCM + GG and ~2.44 mA cm^{-2} for DT-CCM + SG show a clear reduction compared to those of the representative controls (~3.62 mA cm^{-2} for N211 + spin-scoop with an ~700 nm carrier layer of Nafion and ~3.46 mA cm^{-2} for bare N211). Unlike GDE-based MEAs, the DT-CCM MEAs exhibited a clear reduction in hydrogen crossover with N211 + GG showing ~25% and N211 + SG showing ~33% (Fig. 5C).

Table 3 Summary of performance data from Fig. 5 for MEAs with N211 and DT-CCM

	OCV (V)	ECSA ($m^2\ g^{-1}$)	HFR at 1000 mA cm^{-2} ($m\Omega\ cm^2$)	H_2 crossover ($mA\ cm^{-2}$)
N211 DT-CCM	0.957	37	68	3.46
N211 with spin-scoop DT-CCM	0.948	37	56	3.62
N211 + GG DT-CCM	0.950	31	59	2.73
N211 + SG DT-CCM	0.966	42	74	2.44

The reduction in hydrogen crossover with the integration of CVD graphene and almost no changes in cell power density for N211 provides an opportunity to move towards thinner membranes such as N12 (nominal thickness ~12 μm) to further enhance the cell power density with the eventual aim of lowering the cost for hydrogen fuel cell.

Hence, we proceeded to use DT-CCM process with N12 membranes to fabricate and test MEAs with and without CVD graphene (Fig. 6 and Table 4). Consistent with observations for N211 MEAs in Fig. 2–5, the polarization curves in Fig. 6A appear similar, with N12 + GG MEA showing slightly lower performance than the others. The ECSA for N12 + SG MEA exhibited a higher value of ~42 $m^2\ g^{-1}$ than the other three MEAs ~35 $m^2\ g^{-1}$ but is still within the error estimates (Fig. 6E). Notably, we observed lower HFR for N12 (Fig. 6F) compared to N211 (Fig. 5F) as one would expect for a thinner membrane. The HFR values were ~50 $m\Omega\ cm^2$ for N12,

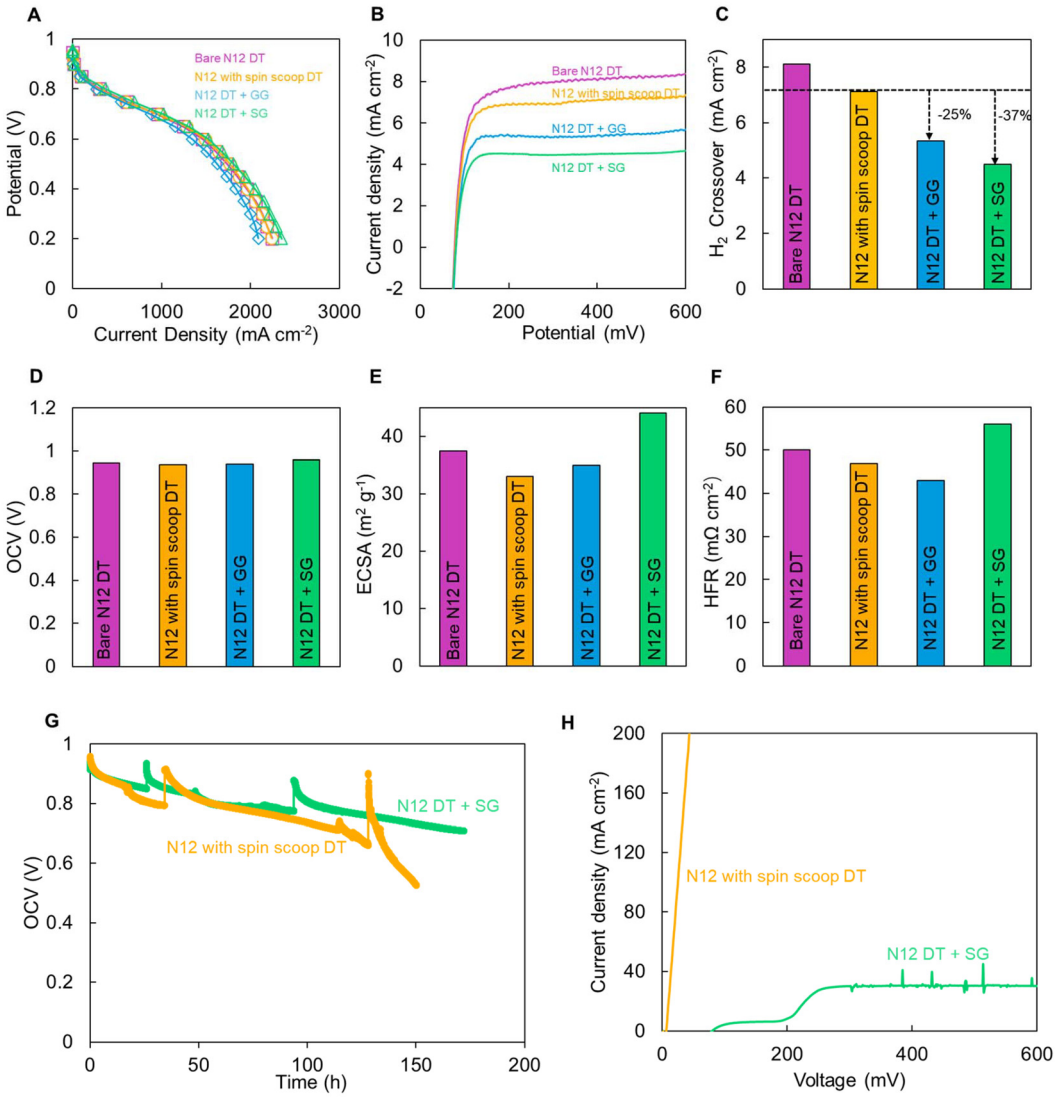

Fig. 6 Comparison of fuel cell performance under 80 °C, 100% RH and 150 kPa_{abs} conditions among MEAs with bare N12 membranes, N12 with spin-scoop carrier layer, N12 + GG (commercially avaialable CVD graphene), and N12 + SG (lab-grown CVD graphene), prepared using decal transfer: (A) polarization curves, (B) current density as a function of voltage, and (C) H_2 crossover extracted from (B) at 0.4 V. (D) Open-circuit voltage (OCV), (E) electrochemically active surface area (ECSA), and (F) high-frequency resistance (HFR) at 1000 mA cm^{-2}. (G) OCV durability tests of N12 with SG DT and N12 with spin-scoop DT samples under 90 °C, 30% RH, and 100 kPa_{abs} conditions, and gas flow rates of 125/500 sccm (H_2/air). (H) Hydrogen crossover after the durability test. Note that DT-CCM is abbreviated as DT in this figure. Also see Table 4.

Table 4 Summary of performance data from Fig. 6 for MEAs with N12 and DT-CCM

	OCV (V)	ECSA ($m^2\ g^{-1}$)	HFR at 1000 mA cm^{-2} (mΩ cm^2)	H_2 crossover (mA cm^{-2})
N12 DT	0.946	37	50	8.10
N12 with spin-scoop DT	0.938	33	47	7.11
N12 with GG DT	0.939	35	43	5.34
N12 with SG DT	0.958	44	56	4.49

~47 mΩ cm^2 for N12 with a spin-scoop carrier layer, ~43 mΩ cm^2 for N12 + GG and ~56 mΩ cm^2 for N12 + SG. A minor but relatively high ECSA of ~44 $m^2\ g^{-1}$ for N12 + SG MEA may compensate for its higher HFR, resulting in polarization behavior similar to those of the other samples.

Fig. 6B and C present the hydrogen crossover curves for N12 membranes with two controls N12 and N12 with the spin-scoop Nafion carrier layer exhibiting crossover of 8.10 mA cm^{-2} and 7.11 mA cm^{-2}, respectively. The lower hydrogen crossover for N12 + spin-scoop Nafion in comparison with N12 is within expectation as the addition of the ~700 nm spin-scoop layer increased the thickness of the N12 membrane by at least ~6%. Interestingly, the H_2 crossover values after integration of monolayer CVD graphene (Fig. 5C and Table 4) for N12 + GG ~5.34 mA cm^{-2} and for N12 + SG ~4.49 mA cm^{-2} were much lower than for bare N12 (~8.10 mA cm^{-2}) and N12 + spin-scoop Nafion control (~7.11 mA cm^{-2}). Specifically, the N12 + GG exhibited ~34% lower crossover than bare N12 and ~25% lower than N12 + spin-scoop Nafion, while N12 + SG exhibited reductions of about ~44% and ~37%, respectively. These results further support the findings from the N211 membranes using the DT-CCM method that the integration of CVD graphene monolayer with PEMs (albeit with some correlation with the support resistance acting in series with CVD graphene for protons) can enable H_2 crossover reduction with minimal impact on fuel cell performance.[1,3,53] Although one may expect larger H_2 crossover reduction with an identical CVD graphene layer on a thin membrane (N12) compared to a thicker membrane (N211), we only observed incremental improvement in this study. The reason is unclear and will be investigated in the future.

Finally, we performed the MEA durability tests by recording a drop in the cell OCV for the N12 + spin-scoop and N12 + SG to assess the effect of reduced hydrogen crossover with CVD graphene incorporation. The accelerated durability tests were conducted at a low relative humidity of ~30% and an elevated cell temperature of 90 °C under ambient backpressure to accelerate membrane chemical degradation *via* oxidative stress induced by crossed over hydrogen and oxygen. Reduced gas crossover by graphene layer is anticipated to decrease the degradation rate. Under these conditions, as long as the electrical resistance of the MEA is pristine, only two factors determine the voltage at the OCV: the oxygen reduction activity and the H_2 crossover current.[5] As the membrane ages, some degradation products can poison the Pt catalyst and reduce the oxygen reduction activity leading to OCV decay. Fig. 6G exhibits the degradation of the cell OCV with time for both the N12 + spin-scoop Nafion and N12 + SG MEAs recorded under identical operating conditions. The N12 + SG sample exhibited a slower degradation rate (~1.2 mV h^{-1}) compared with the control N12 + spin-scoop Nafion DT sample (~2.8 mV h^{-1}). The cell OCV recording was interrupted due to gas run-off events. We also recorded hydrogen crossover at the end of the cell OCV degradation test (Fig. 6H) and observed significantly lower hydrogen crossover for N12 + SG in comparison with that of the N12 + spin-scoop Nafion control. After 150 h, a clear indicator of MEA failure was an abnormally high hydrogen crossover. For the N12 + SG sample, the hydrogen crossover current density increased from ~4.49 mA cm^{-2} to ~30 mA cm^{-2}. In contrast, the N12 + spin-scoop Nafion control showed a dramatic increase from ~7.11 mA cm^{-2} to over ~200 mA cm^{-2}, with a linear increase in the crossover current – an indication of pinhole formation. These results clearly demonstrate that the incorporated CVD graphene layer enhanced the durability of the N12 membrane.

Conclusions

In this study, we examined three different approaches to MEA fabrication—the use of GDE, DS-CCM, and DT-CCM—and evaluated their influence for both bare and graphene-modified PFSA membranes (N211 and N12). All three approaches resulted in similar fuel cell performance for control membranes, justifying their wide community usage. However, in our case we find that manual control and fabrication of low-active-area CCM is challenging. Even though the GDE and DT-CCM approaches resulted in the similar performance, when applied to graphene membranes the GDE samples did not show any crossover reduction relative to the bare membranes. These observations suggest that during GDE fabrication the electrode layer mechanically damages or disrupts the CVD graphene layer during hot-pressing, thereby compromising graphene's barrier properties. Further optimization of GDE pressing conditions (low temperature and pressure) resulted in crossover reduction and the effect of CVD graphene became more apparent in the GDE samples, further supporting this interpretation.

In contrast, when graphene-modified membranes were assembled using the DT-CCM method, both the PEM + GG and PEM + SG effectively reduced H_2 crossover without negatively affecting fuel cell performance. For the N211 membrane, the N211 + SG sample exhibited the largest reduction (~33%) relative to the spin-scoop control, while for the thinner N12 membrane, the reduction was ~37%. These improvements are attributed to the atomically thin graphene layer functioning as a selective barrier that suppresses H_2 permeation while allowing proton transport and maintaining proton conductivity. Furthermore, durability testing revealed that the CVD graphene improved the long-term stability of the N12 membrane with an OCV degradation rate of ~1.2 mV h^{-1} in comparison with ~2.8 mV h^{-1} for the control.

Overall, the decal transfer (DT-CCM) method proved to be the most suitable approach for integrating graphene layers with PFSA membranes, as it preserved CVD graphene integrity and delivered consistent MEA performance. These findings provide practical guidance for optimizing 2D-material-modified membranes in PEM fuel cells, and enable new advances for PEMs with improved gas-barrier properties, proton transport, and durability toward achieving next-generation energy and electrochemical devices.

Experimental methods

Graphene synthesis

Graphene utilized in this study was synthesized *via* chemical vapor deposition (CVD) under two different conditions *i.e.* graphene synthesized *via* atmospheric pressure (AP) CVD was obtained from General Graphene Corporation LLC (labelled as GG),[24,50,56] and graphene synthesized *via* low pressure (LP) CVD (labelled as SG) was obtained using protocols reported earlier.[1,4,17] Briefly, prior to graphene growth *via* CVD, the copper substrate was carefully cleaned. Polycrystalline Cu foils (HA, 18 μm thick, JX Holdings) were first soaked in acetone and isopropanol (IPA) for 5 min each to remove organic residues, followed by etching in 20 vol% nitric acid (HNO_3) to remove surface oxides.[1,4,17] Finally, foil were thoroughly rinsed with deionized water and air-dried.[1,4,17]

Cleaned Cu foils were loaded into a custom-built hot-walled quartz-tube CVD reactor for graphene growth. Prior to growth, the system was pumped down to base pressure (~14 mTorr) and leak tested (<1 mTorr min^{-1}).[1,4,17] Next, the furnace temperature was increased to 1060 °C (~35 °C min^{-1}) under a flow of 100 sccm H_2 (system pressure ≈4 Torr).[1,4,17] The Cu foil was annealed at 1060 °C in 100 sccm H_2 for 60 min (~4 Torr), after which the H_2 flow rate was increased to 300 sccm for an additional 15 min (~14 Torr).[1,4,17] Graphene growth was achieved by introducing a carbon precursor, CH_4 at 1060 °C for a total of 75 minutes (0.5 sccm CH_4 for first 45 minutes, followed by 1 sccm of CH_4 for additional 30 minutes).[1,4,17] After growth, the furnace was opened and quenched cool to room temperature under H_2 and CH_4.[1,4,17]

CVD graphene transfer to Nafion for proton exchange membrane preparation

Graphene was transferred (from the Cu foil growth substate) onto a Nafion membrane using the spin-scoop method, following established protocols.[1,4,17] Specifically, 5 wt% Nafion was spin-coated on graphene on the Cu foil, Gr|Cu, at 1000 rpm for 1 minute followed by baking at 60 °C for 10 minutes. The spin coating step was repeated 3 times with intermediate baking of 10 minutes with a final baking of 30 minutes at 60 °C to completely remove the solvents.[1,4,17] Next, Cu was etched away from 0.2 M ammonium persulfate (APS) solution and the resulting Nafion (spin-coated)|Gr stack was transferred to float on water, followed by 30 minutes floating on 0.1 M HCl to minimize the residual cation contamination in Nafion carrier layer by replacing them with protons and a 10 minute DI water float before scooping on Nafion (N211 ~25 μm and PTFE reinforced[15] N12 ~12 μm) affixed to a PTFE sheet.[1,4,17] The Nafion|Gr|Nafion (spin-coated) stack was dried under ambient atmosphere for 30 minutes and baked at 60 °C overnight.[1,4,17] A Nafion (spin-scoop)|Nafion control membrane was prepared using Cu foil (with no graphene) using the same approach.[1,4,17] For N211, the IEC value was ~0.91 meq g^{-1} and for the N12 sample (effective EW is 850), effective IEC was ~1.2 meq g^{-1}.

Fabrication of membrane–electrode assemblies (MEAs)

Three different methods were used to fabricate membrane–electrode assemblies (MEAs): (1) gas diffusion electrode (GDE), (2) directly sprayed catalyst-coated membrane (DS-CCM), and (3) decal transfer (DT)-CCM using the same catalyst ink. The catalyst ink was prepared by dispersing Pt/C catalyst (50% Pt on high surface area Ketjenblack EC-300J, Fuel Cell Store) in a water/isopropanol mixture (1 : 1 by weight) containing 20 wt% Nafion solution (D2021, Ion Power, dried into powders and then redispersed in the same solvent) and sonicated and stirred to achieve a homogeneous ink.[76,77]

The three methods differ by the substrate onto which the catalyst was coated (see Fig. 1). For the GDE method, the catalyst ink was sprayed onto gas diffusion layers (GDLs), and the resulting GDEs were hot-pressed with membranes (Nafion|Gr and Nafion) at 250 psi and 150 °C for 3 min to form MEAs. For the DS-CCM method, the catalyst ink was directly sprayed onto the membrane, dried, and then hot-pressed at 250 psi and 150 °C for 3 min after securing the catalyst area with PTFE sheets. For the decal transfer (DT)-CCM method, the catalyst ink was sprayed onto a PTFE film, which was then hot-pressed with the membrane at 250 psi and 150 °C for 3 min; after cooling, the PTFE film was carefully peeled off, yielding a DT-CCM. For both DS-CCMs and DT-CCMs, GDLs were subsequently hot-pressed onto the CCM at 125 psi and 120 °C for 1 min to complete the MEA fabrication. In all cases, the geometric active area was ~1 cm^2 with a loading of 0.2 mg cm^{-2} of Pt.

Prior to cross-sectional SEM imaging, the membrane electrode assemblies (MEAs) fabricated *via* DT and GDE routes were cooled in liquid nitrogen and fractured to expose their cross-sections. The resulting samples were mounted and directly imaged with a Zeiss Merlin scanning electron microscope, eliminating the need for conductive metal deposition. The thickness of N211 after processing was as follows: GDE hot-press: ~23.75 μm, DT-CCM: ~26.67 μm, and CCM: ~25.92 μm.

Fuel-cell testing

Standard fuel cell tests were performed using a Scribner Inc. 850e test station, and cell test fixtures (Fuel Cell Technologies 5 cm^2 with single serpentine gas channels). PTFE sheets were used to mask the cell fixture area to be ~1 cm^2 and desired compression (125 psi). Polarization curves were collected by sweeping voltage from 0.2 V to open-circuit-voltage (OCV) at an interval of 0.05 V, and current was allowed to stabilize for 1 minute before recording the data. The cell was operated under standard conditions (temperature: ~80 °C, relative

humidity: 100%, and backpressure: ~150 kPa_{abs}), with ~125 sccm hydrogen gas (at the anode) and ~500 sccm air (at the cathode), respectively. Notably, graphene layer is closer to the anode side.[1]

Linear sweep voltammetry (LSV) was used to measure hydrogen crossover.[78] Humidified hydrogen gas (~125 sccm) was fed through the cathode flow channel and humidified nitrogen gas (~125 sccm) was fed to the anode. A Gamry potentiostat (Gamry Reference 3000) was used to sweep the voltage from 0.04 V to 0.7 V *vs.* SHE (Standard Hydrogen Electrode) at a scan rate of 2 mV s^{-1} at 80 °C and 150 kPa_{abs}. Currents measured from an LSV scan are due to the oxidation of hydrogen gas at the anode that leaked across the membrane. From a plot of current density *vs.* voltage, the hydrogen crossover limiting current density was reported at a DOE standard of ~0.4 V. The electrochemically active surface area of cathodes (ECSA) was measured at ~30 °C and ambient pressure from hydrogen adsorption/desorption cyclic voltammograms using an external potentiostat (Gamry Reference 3000). After purging the anode with H_2 and cathode with N_2, a hydrogen oxidation/reduction cyclic voltammogram was generated between 0.04 V and 1 V (*vs.* SHE) at 100 kPa_{abs}, 30 °C, and 100% relative humidity, with a sweep rate of 20 mV s^{-1}. The hydrogen adsorption charge density (Q, with units of C cm^{-2}) was calculated from the integrated area above the hydrogen adsorption portion of the voltammogram (between 0.1 V and 0.4 V). The ECSA (with units of cm^2 $g_{Pt}{}^{-1}$) was calculated[79] using the equation:

$$\mathrm{ECSA} = \frac{Q}{\Gamma \cdot L},$$

where Γ is the charge density for a monolayer of H_2 on Pt (~210 μC cm^{-2}), L is the Pt loading (mg cm^{-2}), and Q is the hydrogen adsorption charge density (C cm^{-2}).

Author contributions

P. R. K. conceived and supervised the project. X. F. fabricated the MEAs and tested them with P. C. and R. A (Fig. 4C). A. T. synthesized CVD graphene. A. K. provided N12 PEMs and regular input on research results, contributed to discussions, and detailed technical input. X. F. and P. R. K. wrote the manuscript with input and discussion with all co-authors.

Conflicts of interest

P.R.K. acknowledges stake in a company aimed at commercializing 2D materials.

Data availability

All data are available within the article in the form of tables, figures, and text.

Acknowledgements

This work is partially supported by the U.S. Department of Energy's Office of Energy Efficiency and Renewable Energy (EERE) under the Hydrogen and Fuel Cell Technologies Office Award (number DE-EE0011106), in part by the National Science Foundation CAREER Award (1944134) to P.R.K, and in part by the U.S. Department of Energy Early Career Research Program Award (DE-SC0022915) to P.R.K. We acknowledge General Graphene Corporation LLC for providing CVD graphene on Cu foil. We acknowledge Dr. Ranadip Goswami for detailed reading of proofs.

References

1 N. K. Moehring, A. B. Mansoor Basha, P. Chaturvedi, T. Knight, X. Fan, P. N. Pintauro, M. S. H. Boutilier, K. Karan and P. R. Kidambi, *Nano Lett.*, 2025, **25**, 1165–1176.
2 P. R. Kidambi, P. Chaturvedi and N. K. Moehring, *Science*, 2021, **374**, 7687.
3 N. K. Moehring, P. Chaturvedi, P. Cheng, W. Ko, A. P. Li, M. S. H. Boutilier and P. R. Kidambi, *ACS Nano*, 2022, **16**, 16003–16018.
4 N. K. Moehring, A. E. Naclerio, P. Chaturvedi, T. Knight and P. R. Kidambi, *Nanoscale*, 2024, **16**, 6973–6983.
5 P. Q. Ngo, Y. Zhang, W. Gu, K. S. Reeves, L. Amichi, D. A. Cullen and A. Kongkanand, *J. Electrochem. Soc.*, 2026, **173**, 014503.
6 P. Chaturvedi, P. Cheng, S. M. Hus, M. Coupin, A. Li, J. Warner, M. S. H. Boutilier and P. R. Kidambi, *Adv. Mater.*, 2026, **38**, e10609.
7 X. H. Yan, R. Wu, J. B. Xu, Z. Luo and T. S. Zhao, *J. Power Sources*, 2016, **311**, 188–194.
8 M. Komma, A. T. S. Freiberg, D. Abbas, F. Arslan, M. Milosevic, S. Cherevko, S. Thiele and T. Böhm, *ACS Appl. Mater. Interfaces*, 2024, **16**, 30.
9 N. Metzger, I. Vlassiouk, S. Smirnov, G. Mariscal, R. Spragg and X. Li, *J. Electrochem. Energy Convers. Storage*, 2023, **20**, 020903.
10 S. Bukola and S. E. Creager, *ECS Meeting Abstracts*, 2019, **MA2019-02**, 1507.
11 S. M. Lyth, T. Bayer, K. Sasaki, E. M. Can, B. Cunning, M. Nishihara and A. Mufundirwa, *ECSMA*, 2024, **MA2024-02**, 2935.
12 M. Sahoo, V. Kalangi, M. Perez-page, R. R. Nair and S. Holmes, *ECS Meeting Abstracts*, 2018, MA2018-02, 1432.
13 J. Chen, J. J. Bailey, L. Britnell, M. Perez-Page, M. Sahoo, Z. Zhang, A. Strudwick, J. Hack, Z. Guo, Z. Ji, P. Martin, D. J. L. Brett, P. R. Shearing and S. M. Holmes, *Nano Energy*, 2022, **93**, 106829.
14 H. Su and Y. H. Hu, *Energy Sci. Eng.*, 2021, **9**, 958–983.
15 P. Q. Ngo, Y. Zhang, W. Gu, K. S. Reeves, L. Amichi, D. Cullen and A. Kongkanand, *J. Electrochem. Soc.*, 2026, DOI: 10.1149/1945-7111/ae320f.

16 S. Kim and Y. M. Lee, *Curr. Opin. Chem. Eng.*, 2023, **39**, 100893.
17 P. Chaturvedi, N. K. Moehring, T. Knight, R. Shah, I. Vlassiouk and P. R. Kidambi, *Mater. Adv.*, 2023, **4**, 3473–3481.
18 P. Chaturvedi, N. K. Moehring, P. Cheng, I. Vlassiouk, M. S. H. Boutilier and P. R. Kidambi, *J. Mater. Chem. A*, 2022, **10**, 19797–19810.
19 Y. Jiang, J. Ma, C. Yang and S. Hu, *J. Phys. Chem. Lett.*, 2021, **12**, 12376–12383.
20 W. Zhang, X. Liu, B. Chen, L. Sun, Z. Liu and G. F. Schneider, *ACS Appl. Mater. Interfaces*, 2025, **17**, 63438–63447.
21 J. Yang, Z. Zhuang, N. Wu, D. Zhang, B. Feng, D. Hou, L. Wang, J. Yang, Z. Zhuang, N. Wu, D. Zhang, B. Feng, L. Wang and D. Hou, *Small*, 2025, **21**, 2502473.
22 J. Tong, Y. Fu, D. Domaretskiy, F. Della Pia, P. Dagar, L. Powell, D. Bahamon, S. Huang, B. Xin, R. N. Costa Filho, L. F. Vega, I. V. Grigorieva, F. M. Peeters, A. Michaelides and M. Lozada-Hidalgo, *Nature*, 2024, **630**, 619–624.
23 O. J. Wahab, E. Daviddi, B. Xin, P. Z. Sun, E. Griffin, A. W. Colburn, D. Barry, M. Yagmurcukardes, F. M. Peeters, A. K. Geim, M. Lozada-Hidalgo and P. R. Unwin, *Nature*, 2023, **620**, 782–786.
24 S. Kutagulla, D. King, P. Carmichael, C. R. Barnett, U. Misra, P. R. Kidambi, M. Kumar and D. Akinwande, *MRS Bull.*, 2025, **50**, 1417–1425.
25 W. Zhang, M. Makurat, X. Liu, B. Chen, Y. Li, X. Liu, T. J. F. Kock, A. Jiao, G. Jiang, C. Leist, C. Maheu, H. Sezen, D. Calvani, I. Eren, L. Jiang, F. Buda, H. Qi, J. P. Hofmann, X. Feng, U. Kaiser, L. Sun, Z. Liu, A. Kuc, T. Heine and G. F. Schneider, *Nat. Commun.*, 2025, **16**, 10857.
26 P. Chaturvedi, A. E. Naclerio, S. M. Hus, I. V. Vlassiouk, N. Lavrik, M. Checa, L. Collins, A. P. Li and P. R. Kidambi, *Adv. Mater.*, 2025, e11868.
27 A. O. Krasnova, N. V. Glebova, A. G. Kastsova, A. O. Pelageikina, A. V. Redkov, M. V. Tomkovich, A. A. Nechitailov, A. O. Krasnova, N. V. Glebova, A. G. Kastsova, A. O. Pelageikina, A. V. Redkov, M. V. Tomkovich and A. A. Nechitailov, *Nanomaterials*, 2024, **14**, 922.
28 N. Metzger, I. Vlassiouk, S. Smirnov, G. Mariscal, R. Spragg and X. Li, *J. Electrochem. Energy Convers. Storage*, 2023, **20**, 020903.
29 S. Kutagulla, P. Carmichael, M. Coupin, D. Mutyala, N. Ignacio, N. H. Le, I. T. Caldino Bohn, J.-W. Kim, K. S. Mason, J. Warner, N. Aluru, B. A. Korgel, Z. A. Page and D. Akinwande, *ACS Nano*, 2025, **19**, 9422–9431.
30 D. A. Gribble, P. Cheng, V. G. Pol and P. R. Kidambi, *ACS Appl. Mater. Interfaces*, 2025, **17**, 55554–55563.
31 Z. Wang, J. Yang, M. Yong, X. Zeng, M. Tebyetekerwa, K. Sun, C. Bie, C. Xing, H. Wang, D. V. Andreeva, K. S. Novoselov and X. Zhang, *Chem. Rev.*, 2025, **125**, 6753–6818.
32 A. E. Naclerio, P. Cheng, S. M. Hus, J. T. Diulus, M. Checa, I. Vlassiouk, W. H. Fissell, M. Coupin, J. Warner, L. Collins, A. Kolmakov, A. P. Li and P. R. Kidambi, *Nano Lett.*, 2025, **25**, 3221–3232.
33 J. T. Diulus, A. E. Naclerio, J. A. Boscoboinik, A. R. Head, E. Strelcov, P. R. Kidambi and A. Kolmakov, *J. Phys. Chem. C*, 2024, **128**, 7591–7600.
34 P. Bishnoi, K. Mishra, S. S. Siwal, V. K. Gupta and V. K. Thakur, *Adv. Energy Sustainability Res.*, 2024, **5**, 2300266.
35 D. Calvani, B. Kreupeling, G. J. A. Sevink, H. J. M. de Groot, G. F. Schneider and F. Buda, *J. Phys. Chem. C*, 2024, **128**, 3514–3524.
36 A. E. Naclerio and P. R. Kidambi, *Adv. Mater.*, 2023, **35**, 2207374.
37 A. F. Ordorica, P. Cheng, P. Chaturvedi, P. T. Cummings and P. R. Kidambi, *ACS Nano*, 2025, **19**, 42222–42241.
38 N. A. A. Qasem and G. A. Q. Abdulrahman, *Int. J. Energy Res.*, 2024, 7271748.
39 P. R. Kidambi, C. Weijtens, J. Robertson, S. Hofmann and J. Meyer, *Appl. Phys. Lett.*, 2015, **106**, 063304.
40 D. A. Gribble, P. Cheng, V. G. Pol and P. R. Kidambi, *ACS Appl. Mater. Interfaces*, 2025, **17**, 55554–55563.
41 G. Romaniak, P. Cheng, K. Dybowski, P. Kula and P. R. Kidambi, *Mater. Res. Express*, 2023, **10**, 105101.
42 A. I. Aria, P. R. Kidambi, R. S. Weatherup, L. Xiao, J. A. Williams and S. Hofmann, *J. Phys. Chem. C*, 2016, **120**, 2215–2222.
43 B. Dlubak, P. R. R. Kidambi, R. S. S. Weatherup, S. Hofmann and J. Robertson, *Appl. Phys. Lett.*, 2012, **100**, 173113.
44 P. Cheng, N. K. Moehring, J. C. Idrobo, I. N. Ivanov and P. R. Kidamb, *Nanoscale*, 2021, **13**, 2825–2837.
45 G. Li, T. Xu, S. Luo, Q. Wang, X. Li, D. Xing, P. Ming, B. Li and C. Zhang, *J. Power Sources*, 2024, **623**, 235415.
46 L. Wang, C. M. Williams, M. S. H. Boutilier, P. R. Kidambi and R. Karnik, *Nano Lett.*, 2017, **17**, 3081–3088.
47 L. Wang, M. S. H. Boutilier, P. R. Kidambi, D. Jang, N. G. Hadjiconstantinou and R. Karnik, *Nat. Nanotechnol.*, 2017, **12**, 509–522.
48 A. Kuruvila, P. R. Kidambi, J. Kling, J. B. Wagner, J. Robertson, S. Hofmann and J. Meyer, *J. Mater. Chem. C*, 2014, **2**, 6940.
49 P. R. Kidambi, M. S. H. Boutilier, L. Wang, D. Jang, J. Kim and R. Karnik, *Adv. Mater.*, 2017, **29**, 1605896.
50 P. Chaturvedi, N. K. Moehring, P. Cheng, I. Vlassiouk, M. S. H. Boutilier and P. R. Kidambi, *J. Mater. Chem. A*, 2022, **10**, 19797–19810.
51 P. R. Kidambi, R. A. Terry, L. Wang, M. S. H. Boutilier, D. Jang, J. Kong and R. Karnik, *Nanoscale*, 2017, **9**, 8496–8507.
52 P. R. Kidambi, D. D. Mariappan, N. T. Dee, A. Vyatskikh, S. Zhang, R. Karnik and A. J. Hart, *ACS Appl. Mater. Interfaces*, 2018, **10**, 10369–10378.
53 M. S. H. Boutilier, D. Jang, J.-C. Idrobo, P. R. Kidambi, N. G. Hadjiconstantinou and R. Karnik, *ACS Nano*, 2017, **11**, 5726–5736.
54 A. Kudo, S. A. Steiner, B. C. Bayer, P. R. Kidambi, S. Hofmann, M. S. Strano and B. L. Wardle, *J. Am. Chem. Soc.*, 2014, **136**, 17808–17817.

55 P. Cheng, J. Espano, A. Harkaway, A. E. Naclerio, N. K. Moehring, P. Braeuninger-Weimer and P. R. Kidambi, *ACS Appl. Mater. Interfaces*, 2022, **14**, 41328–41336.
56 M. K. Debe, *Nature*, 2012, **486**, 43–51.
57 T. Cebo, A. I. Aria, J. A. Dolan, R. S. Weatherup, K. Nakanishi, P. R. Kidambi, G. Divitini, C. Ducati, U. Steiner and S. Hofmann, *Appl. Phys. Lett.*, 2017, **111**, 253103.
58 P. R. Kidambi, G. D. Nguyen, S. Zhang, Q. Chen, J. Kong, J. Warner, A.-P. Li and R. Karnik, *Adv. Mater.*, 2018, **1804977**, 1804977.
59 H. Butt, P. R. Kidambi, B. Dlubak, Y. Montelongo, A. Palani, G. A. J. J. Amaratunga, S. Hofmann and T. D. Wilkinson, *Adv. Opt. Mater.*, 2013, **1**, 869–874.
60 P. Cheng, F. Fornasiero, M. L. Jue, W. Ko, A. P. Li, J. C. Idrobo, M. S. H. Boutilier and P. R. Kidambi, *Nat. Commun.*, 2022, **13**, 6709.
61 P. R. Kidambi, R. Blume, J. Kling, J. B. Wagner, C. Baehtz, R. S. Weatherup, R. Schloegl, B. C. Bayer and S. Hofmann, *Chem. Mater.*, 2014, **26**, 6380–6392.
62 P. R. Kidambi, C. Ducati, B. Dlubak, D. Gardiner, R. S. Weatherup, M.-B. Martin, P. Seneor, H. Coles and S. Hofmann, *J. Phys. Chem. C*, 2012, **116**, 22492–22501.
63 P. Cheng, M. M. Kelly, N. K. Moehring, W. Ko, A. P. Li, J. C. Idrobo, M. S. H. Boutilier and P. R. Kidambi, *Nano Lett.*, 2020, **20**, 5951–5959.
64 R. Degl'Innocenti, D. S. Jessop, Y. D. Shah, J. Sibik, A. Zeitler, P. R. Kidambi, S. Hofmann, H. E. Beere and D. A. Ritchie, in *Terahertz, RF, Millimeter, and Submillimeter-Wave Technology and Applications VII*, ed. L. P. Sadwick and C. M. O'Sullivan, 2014, vol. 8985, p. 89851E.
65 M. Kratzer, B. C. Bayer, P. R. Kidambi, A. Matković, R. Gajić, A. Cabrero-Vilatela, R. S. Weatherup, S. Hofmann and C. Teichert, *Appl. Phys. Lett.*, 2015, **106**, 103101.
66 P. R. Kidambi, D. Jang, J.-C. Idrobo, M. S. H. Boutilier, L. Wang, J. Kong and R. Karnik, *Adv. Mater.*, 2017, **29**, 1700277.
67 R. Degl'Innocenti, D. S. Jessop, Y. D. Shah, J. Sibik, J. A. A. Zeitler, P. R. Kidambi, S. Hofmann, H. E. Beere and D. A. Ritchie, *ACS Nano*, 2014, **8**, 2548–2554.
68 P. Cheng, N. Ferrell, S. M. Hus, N. K. Moehring, M. J. Coupin, J. Warner, A. P. Li, W. H. Fissell and P. R. Kidambi, *Nano Lett.*, 2024, **25**, 193–203.
69 A. C. Ferrari and D. M. Basko, *Nat. Nanotechnol.*, 2013, **8**, 235–246.
70 P. Cheng, P. Chaturvedi and P. R. Kidambi, *Nano Lett.*, 2026, **26**, 1480–1488.
71 P. R. Kidambi, B. C. Bayer, R. Blume, Z.-J. Wang, C. Baehtz, R. S. Weatherup, M.-G. Willinger, R. Schloegl and S. Hofmann, *Nano Lett.*, 2013, **13**, 4769–4778.
72 R. Blume, P. R. Kidambi, B. C. Bayer, R. S. Weatherup, Z.-J. Wang, G. Weinberg, M.-G. Willinger, M. Greiner, S. Hofmann, A. Knop-Gericke and R. Schlögl, *Phys. Chem. Chem. Phys.*, 2014, **16**, 25989–26003.
73 R. Wang, P. R. Whelan, P. Braeuninger-Weimer, S. Tappertzhofen, J. A. Alexander-Webber, Z. A. Van Veldhoven, P. R. Kidambi, B. S. Jessen, T. Booth, P. Bøggild and S. Hofmann, *ACS Appl. Mater. Interfaces*, 2016, **8**, 33072–33082.
74 J. Carpena-Núñez, J. A. Boscoboinik, S. Saber, R. Rao, J.-Q. Zhong, M. R. Maschmann, P. R. Kidambi, N. T. Dee, D. N. Zakharov, A. J. Hart, E. A. Stach and B. Maruyama, *ACS Nano*, 2019, **13**, 8736–8748.
75 B. C. Steele and A. Heinzel, *Nature*, 2001, **414**, 345–352.
76 K. Waldrop, J. J. Slack, C. Gumeci, J. Parrondo, N. Dale, K. S. Reeves, D. A. Cullen, K. L. More and P. N. Pintauro, *J. Electrochem. Soc.*, 2023, **170**, 024507.
77 X. Fan, X. Xu and P. Pintauro, *J. Power Sources*, 2026, **664**, 238930.
78 J. Zhang, H. Zhang, J. Wu and J. Zhang, *PEM fuel cell testing and diagnosis*, Elsevier Science, 2013.
79 K. Kinoshita and P. Stonehart, in *Modern Aspects of Electrochemistry*, Springer US, Boston, MA, 1977, pp. 183–266.